# Specific-Ion Effects on the Aggregation Mechanisms and Protein–Protein Interactions for Anti-streptavidin Immunoglobulin Gamma-1

Gregory V. Barnett,[†] Vladimir I. Razinkov,[‡] Bruce A. Kerwin,[‡] Thomas M. Laue,[§] Andrea H. Woodka,[∥] Paul D. Butler,[∥] Tatiana Perevozchikova,[†] and Christopher J. Roberts*,[†]

[†]Department of Chemical and Biomolecular Engineering, University of Delaware, Newark, Delaware 19716, United States
[‡]Drug Product Development, Amgen Inc., Seattle, Washington 98119, United States
[§]Department of Molecular, Cellular, and Medical Biosciences, University of New Hampshire, Durham, New Hampshire 03824, United States
[∥]National Institutes of Standards and Technology Center for Neutron Research, Gaithersburg, Maryland 20899, United States

S *Supporting Information*

ABSTRACT: Non-native protein aggregation is common in the biopharmaceutical industry and potentially jeopardizes product shelf life, therapeutic efficacy, and patient safety. The present article focuses on the relationship(s) among protein–protein interactions, aggregate growth mechanisms, aggregate morphologies, and specific-ion effects for an anti-streptavidin (AS) immunoglobulin gamma 1 (IgG1). Aggregation mechanisms of AS-IgG1 were determined as a function of pH and NaCl concentration with sodium acetate buffer and compared to previous work with sodium citrate. Aggregate size and shape were determined using a combination of laser light scattering and small-angle neutron or X-ray scattering. Protein–protein interactions were quantified in terms of the protein–protein Kirkwood–Buff integral (G_{22}) determined from static light scattering and in terms of the protein effective charge (Z_{eff}) measured using electrophoretic light scattering. Changing from citrate to acetate resulted in significantly different protein–protein interactions as a function of pH for low NaCl concentrations when the protein displayed positive Z_{eff}. Overall, the results suggest that electrostatic repulsions between proteins were lessened because of preferential accumulation of citrate anions, compared to acetate anions, at the protein surface. The predominant aggregation mechanisms correlated well with G_{22}, indicating that ion-specific effects beyond traditional mean-field descriptions of electrostatic protein–protein interactions are important for predicting qualitative shifts in protein aggregation state diagrams. Interestingly, while solution conditions dictated which mechanisms predominated, aggregate average molecular weight and size displayed a common scaling behavior across both citrate- and acetate-based systems.
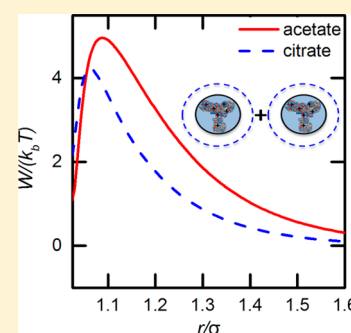
INTRODUCTION

There are over 30 FDA approved monoclonal antibodies (mAbs) for therapeutic use and hundreds of mAbs in biopharmaceutical pipelines.[1] These large, multidomain proteins are attractive drug candidates due to their strong and specific binding to targeted antigens. However, as with many biomacromolecule-based therapeutics, mAbs may encounter stability issues that potentially jeopardize product quality.[2] In general, proteins are labile molecules that can degrade through a variety of pathways in aqueous solution, including fragmentation, isomerization, deamidation, oxidation, and aggregation.[3−6] Irreversible, non-native protein aggregation is one of the most common degradation routes and can potentially occur at any step during the product life cycle of a therapeutic protein; this includes protein expression, purification, final product fill-finish, storage, shipping, and administration.[7,8]

Protein aggregation is a recognized risk factor for drug safety and efficacy.[9−11] Even low levels of aggregates may have the potential to elicit an immune response in patients. This response may be mounted against the therapeutic protein and make future treatments ineffective.[12] The mechanism behind aggregate immune response is complex and involves multiple pathways, and development of models to predict immunogenicity is an ongoing challenge.[13,14] Factors that are known to affect immunogenicity are aggregate concentration, size, epitope, targeted antigen, and patient-specific factors.[9,15] There is not an accepted safe threshold for the amount and size of aggregates for patients. Therefore, minimizing aggregate concentration and size is considered necessary by regulatory agencies to reduce potential risks to patients.[10,11] In the context of this article, the term aggregates denotes net irreversible aggregated species and is further categorized below in later sections to distinguish among aggregates of different average size and shape (or morphology) based on the mechanisms by which they form and grow.

Protein products must be formulated so as to minimize chemical and physical degradation during storage and shipping.

The most common formulation parameters include pH, ionic strength, and the type and concentration of excipients such as buffer species and neutral or charged osmolytes. The conformational stability of proteins (i.e., the Gibbs free energy of unfolding) and aggregation mechanisms and rates can change drastically with pH, salt, and excipient type and concentration.[16−18] There are no robust *a priori* methods to predict aggregation mechanism(s) or unfolding behavior for a given formulation.[19] The mechanism may change significantly with different formulation conditions, and this may affect the growth rate of aggregates as well as the average size, concentration, and morphology of the aggregates.[20−23]

In the case of aggregation, one typically distinguishes between aggregates that are visible or insoluble, subvisible but still very large (characteristic dimensions $\sim 10^3$ nm or larger), and high molecular weight (HMW) soluble species. The latter denotes aggregates that are well-dispersed in the solvent at a molecular level, but this includes stoichiometries that span from dimers to large multimers ($\sim 10-10^2$ monomers).[10,21,24] Relatively little is known regarding how to control or predict which aggregation mechanism(s) will occur or what types of aggregates will result from a given choice of formulation conditions.

Previous work systematically showed the aggregation mechanism changes with pH and [NaCl] for a model protein (aCgn).[21] Aggregates grew through a chain polymerization (CP) mechanism, i.e., growth by monomer addition, under acidic conditions with no added salt, but as the ionic strength increased, the mechanism shifted to primarily association polymerization (AP) and eventually led to phase-separated (PS) aggregates. Prior work also empirically mapped out an aggregation state diagram for anti-streptavidin (AS) immunoglobulin gamma 1 (AS-IgG1) as a function of pH and NaCl concentration.[21] From that work, it was concluded that electrostatic protein−protein interactions at least qualitatively mediated which aggregation mechanism(s) predominated.[20] One striking difference between aggregation mechanisms for aCgn and AS-IgG1 was identified at low pH and salt concentrations, where IgG1 aggregates did not grow significantly beyond small oligomers (dimers, trimers, tetramers). Because aggregation effectively was halted at the initial stages (or at the point of nucleation of stable dimers and small oligomers), this scenario was termed nucleation-dominated (ND). As the pH and or salt concentration increased for AS-IgG1, the aggregate growth mechanism shifted to being dominated by chain polymerization. Upon further increases of the pH toward the pI, or addition of more NaCl, the growth mechanism became a combination of CP and AP. At sufficiently high pH or salt concentration, growth was dominated by AP, and eventually all aggregates underwent rapid phase separation (PS) into macroscopic particles.[21]

While previous work showed pH and NaCl concentration mediated protein−protein electrostatic repulsions, it did not consider that the type of ions in solution might affect the relevant protein−protein interactions and aggregation mechanisms. Specific-ion effects, sometimes referred to as Hofmeister effects, might be anticipated when considering different options for buffer components or the choice of added salts to control properties such as viscosity.[25−28] While measurable Hofmeister effects typically require relatively large salt concentrations ($\sim 0.1-1$ M),[29,30] it was hypothesized in this work that ion-specific effects may manifest even under low salt conditions that are more typical of therapeutic protein products.[31]

The present work provides a systematic comparison of the AS-IgG1 aggregation mechanisms in sodium acetate and sodium citrate buffers. Citrate- and acetate- specific-ion effects were characterized via differences and similarities illustrated in the AS-IgG1 aggregation state diagrams, mass-to-size scaling behaviors that change with aggregate size, and the net protein−protein interactions and protein charge (valence). The results also illustrate the potential utility and limitations of using colloidal models and measured protein−protein interactions and effective surface charges for monomeric proteins to predict how changes in solution conditions will affect the dominant aggregation mechanism(s) and resulting aggregate sizes and morphology.

■ METHODS

Sample Preparation. Anti-streptavadin IgG1 solution (>98% monomer) was provided by Amgen at a concentration of 30 mg/mL. The protein was dialyzed using Spectra/Por 7 tubing (10 kDa MWCO, Spectrum Laboratories, Santa Clara, CA) as previously reported[32] and filtered after dialysis.[20] The dialysate solutions were prepared with distilled, deionized water (Milli-Q filtration system, Millipore, Billerica, MA), in either 5 mM sodium acetate (Fischer Scientific) or 10 mM sodium citrate (Fischer Scientific), with pH adjusted using NaOH (Fischer Scientific). NaCl (Fischer Scientific) was also added gravimetrically to stock solutions after dialysis for conditions that included additional NaCl. The protein concentration was checked after dialysis using UV−vis absorbance at 280 nm (Agilent 8453 UV−vis, Agilent Technologies, Santa Clara, CA), and the IgG1 extinction coefficient was 1.586 mL/mg cm.[21] All solutions were diluted gravimetrically to working concentrations for later use.

Size-Exclusion Chromatography with Inline Multiangle Light Scattering (SEC-MALS). IgG1 samples prepared at 1 mg/mL for a given choice of solution conditions and were incubated isothermally in hermetically sealed HPLC vials (Waters, Milford, MA) for specified incubation times. Once removed from the water bath, a given vial was immediately quenched on ice to rapidly arrest aggregation and was subsequently held at room temperature (20−23 °C) prior to analysis with SEC-MALS. An Agilent 1100 HPLC (Agilent Technologies, Santa Clara, CA) was connected in-line to a Tosoh (Montgomeryville, PA) TSK-Gel 3000xL size-exclusion-column, a multiangle-light-scattering (MALS) DAWN-HELEOS II (Wyatt, Santa Barbara, CA), and a Wyatt Optilab rEX refractive index detector. Samples were injected with an autosampler, and the monomer was separated from the aggregate portion with the SEC column. As the sample eluted from the column, a variable wavelength detector (VWD Agilent technologies, Santa Clara, CA) measured the protein concentration from the absorbance at 280 nm. The sample monomer fraction was determined by integrating chromatograms as previously reported.[22] Following the VWD, the MALS measured light scattering intensity and the RI detector measured the differential refractive index. The latter determined the eluting protein concentration for the monomer and aggregate peaks. All data were collected using ASTRA software and analyzed as previously reported to determine the overall or total weight average molecular weight (M_w^{tot}) of a given sample across the entire chromatogram.[33] The values of M_w^{tot} were also confirmed to be equal to those obtained from batch MALS. For aggregates with radius of gyration (R_g) larger than ~ 15 nm, there was statistically significant angular dependence over the Q

range from light scattering in SEC-MALS and the R_g was determined using ASTRA software.

Protein−Protein Interactions via Laser Light Scattering. Static light scattering was performed using MALS with a microcuvette accessory (Wyatt Technologies, Santa Barbara, CA). Calibration was performed with filtered toluene at a 90° scattering angle. The scattered intensity showed no angular dependence for IgG1 monomer, as expected because the laser wavelength (658.9 nm) is much larger than the size of the IgG1 ($R_g \sim 4.7$ nm).[34] The excess Rayleigh ratio was calculated according to eq 1. A_{inst} is the configuration-specific constant generated by the MALS calibration procedure, which is based on the scattering geometry so as to recover the correct value for the known value of the Rayleigh ratio of toluene for the laser wavelength (λ) and temperature of interest. V and V_0 are the 90° scattering voltages for the sample and buffer, respectively. V_{laser} and V_{dark} are the incident laser voltage and its dark offset. n is the refractive index of the solvent. Equation 1 is based on a ray-tracing algorithm designed for the microcuvette assembly.[35]

$$R_{ex}^{90} = A_{inst} \frac{(V - V_0)}{(V_{laser} - V_{dark})} n^{1.983} \tag{1}$$

The Kirkwood−Buff integral for protein−protein interactions (G_{22}) was determined from a plot of excess Rayleigh ratio and protein concentration (eq 2). K is the canonical light scattering calibration constant which includes dn/dc (0.186 mL/g for this IgG1) and the laser wavelength (658.9 nm). M_2^{app} is the apparent molecular weight, and c_2 is the protein concentration.[44]

$$\frac{R_{ex}^{90}}{K} = M_2^{app} c_2 + M_2 c_2^2 G_{22} \tag{2}$$

In the limit of low c_2 (or more rigorously, when the absolute value of $c_2 G_{22}$ is less than approximately 0.1), one recovers the canonical expression for R_{ex}^{90} in terms of the second osmotic virial coefficient (B_{22}).[36] Under such dilute or weak-interaction conditions, $B_{22} = -2G_{22}$.[37] At higher protein concentrations or when net protein interactions are larger in magnitude, the canonical expression is incorrect and eq 2 should be used. For cases where interactions are so large as to cause G_{22} to change with c_2, eq 2 was used to fit R_{ex}^{90}/K vs c_2 with sliding windows of c_2 to obtain $G_{22}(c_2)$.[65] As described elsewhere, this procedure allows one to obtain numerical values of G_{22} vs c_2 without needing to assume the mathematical form for $G_{22}(c_2)$.[65]

Determination of Radius of Gyration for Small Oligomers with SAXS. Aggregates with a radius of gyration larger than approximately 15 nm showed angular dependence with static light scattering by MALS (see above). For smaller aggregates, the radius of gyration was determined from the Guinier analysis of small-angle X-ray scattering (SAXS) intensity profiles. SAXS experiments were performed on the Cornell High Energy Synchrotron Source (CHESS) beamline G2 with a dual Pilatus 100K-S SAXS/WAXS detector. Samples were oscillated during exposure to minimize radiation damage during the measurement. The data were reduced and analyzed with BioXTAS RAW software.[38]

IgG1 Aggregate Hydrodynamic Radius from Quasi-Elastic Light Scattering. Quasi-elastic light scattering (QELS) was performed using the WyattQELS accessory (Wyatt Technologies, Santa Barbara, CA) installed within the HELEOS II instrument to analyze aggregated samples at low protein concentrations where structure-factor contributions are

minimized. The correlation function was collected by the autocorrelator and exported from ASTRA software. Data were analyzed using nonlinear regression (in Matlab) to fit each correlation function to a cumulant expansion given by eq 3.[39,40]

$$g_2(\tau) = \alpha + \beta \exp(-2Q^2 D_0 \tau)\left(1 + \frac{\mu_2}{2!}\tau^2\right)^2 \tag{3}$$

α is a constant for the short delay-time baseline, β is an instrument-specific constant, D_0 is the self-diffusion coefficient (when protein concentrations are low), τ is the decay time, μ_2 is the second cumulant and is related to the sample polydispersity index, and Q is the scattering vector defined in eq 4 using constants above and the scattering angle, θ.[47,48]

$$Q = \frac{4\pi n}{\lambda} \sin\left(\frac{\theta}{2}\right) \tag{4}$$

Average hydrodynamic radius (R_h) was determined from the Stokes−Einstein relation, eq 5

$$R_h = \frac{k_B T}{6\pi\eta D_0} \tag{5}$$

where k_B is the Boltzmann constant, T is the absolute temperature, and η is the solution viscosity.

IgG1 Net Charge (Valence) via Electrophoretic Light Scattering. Electrophoretic mobility was measured with a Malvern Zetasizer Nano ZS (Malvern Instruments, Malvern, UK) using laser doppler velocimetry (LDV) and phase analysis light scattering (PALS). IgG1 samples at 10 mg/mL were prepared along with corresponding buffers. Folded capillary cells (Malvern Instruments, part no. DTS 1061) were filled with buffer, and 90 μL of protein sample was pipetted with a gel electrophoresis tip to the bottom of the cell near the scattering volume.

As the IgG1 molecules move in the electric field (E), the scattered light produces a phase shift as a result of the Doppler effect.[41−43] Data were collected using the multimodal standard operating procedure in the Zetasizer DTS software. Poly-(ethylene glycol) (PEG) with a molecular weight of 35 kDa was used as an electro-osmotic flow tracer. PEG 35 kDa was chosen because it is a neutral molecule and has a hydrodynamic radius comparable to that of IgG1. The phase shift (φ) as a function of time (t) was collected for a minimum of four different electric field strengths with IgG1 and PEG. Velocity (v) was determined from linear regression of the phase shift plotted against time, using eq 6.[43]

$$\frac{d\varphi}{dt} = Q \cdot v \tag{6}$$

Electrophoretic mobility (μ) and 95% confidence intervals were determined from linear regression (in Matlab) of IgG1 velocity defined as ($v = v_{sample} - v_{PEG}$) vs E. Multiple field strengths were used in an attempt to provide more accurate determinations of v, given that proteins are much smaller than typical colloidal particles for which the PALS method was originally developed.[44] IgG1 effective charge (Z_{eff}) was determined from the mobility using eq 7.[44] D_0 is the self-diffusion coefficient for IgG1 monomer, which is determined from separate QELS measurements as described above, and e is the charge of an electron. Additional details regarding electrophoretic mobility measurements are provided in Supporting Information.

$$Z_{\text{eff}} = \mu \frac{k_B T}{D_0 e} \tag{7}$$

Small-Angle Neutron Scattering (SANS). Small-angle neutron scattering was performed on the NGB 10 m beamline at the NIST Center for Neutron Research (Gaithersburg, MD). All samples were measured using three configurations: 1 m sample-to-detector distance (SDD) with 5 Å neutrons, 4 m SDD with 5 Å neutrons, and 4 m SDD with 16 Å neutrons. The data were corrected for detector background and sensitivity as well as the scattering contribution from empty titanium cells. The protein scattering profiles were also normalized by incident beam flux, and the raw intensities were placed on an absolute scale using direct beam measurements. All data were reduced and analyzed using Igor Pro NCNR software with standard methods.[45]

Protein samples were prepared for conditions that formed aggregates via the different growth mechanisms in both citrate and acetate buffers as described above. Aggregates were separated from the monomer on a semiprep SEC column (Waters, Milford, MA). Aggregate fractions eluting from the column were concentrated and buffer exchanged to conditions in D_2O rather than H_2O so as to achieve better scattering contrast and reduce incoherent background scattering. For each sample, the buffer was matched to the original NaCl concentration and buffer concentration, and the pD was matched to the pH of the original solutions.[46] The total scattering is given by eq 8. $I(Q)$ is the scattered intensity, $\Delta\rho$ is the neutron scattering-length-density difference between the protein and buffer, V is the molecular volume of the protein, $P(Q)$ is the particle form factor, and $S(Q)$ is the structure factor.[47] Scattering was performed on samples with aggregate concentrations between 3 and 6 mg/mL to minimize contributions from the structure factor. In subsequent analysis, $S(Q)$ was assumed to be effectively 1.

$$I(Q) = \frac{(\Delta\rho)^2 V}{N_A} c_2 M_w\, P(Q)\, S(Q) \tag{8}$$

■ RESULTS

Aggregation Mechanism(s) from SEC-MALS. Differences between aggregation mechanism(s) were evaluated using SEC-MALS. For each pH, NaCl concentration, and choice of buffer species, isothermal incubations were performed at temperatures to achieve monomer loss half-lives of approximately 2 h. These incubation conditions allowed for adequate temperature control when removing samples from the incubator for multiple time points, which reduced artificial lag times due to sample heating on much shorter time scales.[48,49] SEC-MALS analysis was performed to quantify the monomer fraction (m) and total molecular weight (M_w^{tot}) of each sample (which includes all aggregate species and monomer) as a function of the sample incubation time at elevated temperature. Monomer fraction was determined from a given SEC chromatogram. It is defined as the monomer peak area for a given sample divided by that for the initial, unheated sample. M_w^{tot} was determined from a weighted summation over M_w slices in from the chromatogram as described above (cf. Methods) and elsewhere.[33]

Differential scanning calorimetry (DSC) measurements were also performed as a function of pH and NaCl concentration to provide reference temperatures for selecting incubation

temperatures, as aggregation rates under accelerated conditions are well-known to be sensitive to changes in calorimetric peak temperatures (T_m).[50] Prior work established that Fab unfolding mediated aggregation for AS-IgG1 under comparable solution conditions.[21] All incubation temperatures used here were below the lowest T_m value for a given pH and NaCl concentration. Doing so helps to avoid switches from unfolding-limited to aggregation-limited mechanisms as one crosses T_m.[19] While rates for aggregate nucleation, growth, and coalescence may change with temperature, the categories for aggregation mechanism that are used here are expected to be qualitatively similar since the incubation temperatures differed only by a few degrees for a given case (ND, CP, AP, etc.). Determining the detailed temperature dependence of the aggregation kinetics for this IgG1 was beyond the scope of this article, but this will be reported in future work to be described elsewhere. See Supporting Information for the temperatures for incubation of each of the isothermal aggregation experiments used in constructing Figure 1 and peak temperatures from DSC thermograms.
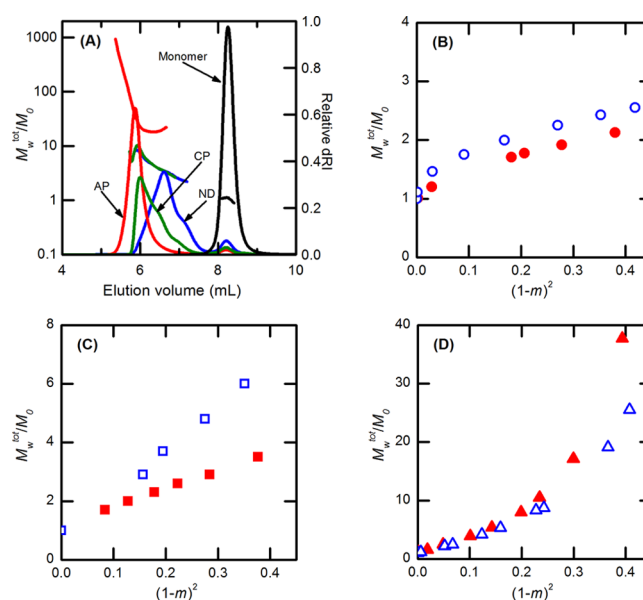

Figure 1. SEC-MALS results distinguishing different aggregation mechanism. (A) Representative chromatograms for IgG1 monomer, the nucleation-dominated (ND), chain polymerization (CP), and association polymerization (AP) growth mechanisms. M_w^{tot} vs $(1 - m)^2$ plots showing aggregation through (B) ND, (C) CP, and (D) AP growth mechanisms. Blue open symbols represent aggregates from 5 mM citrate buffer, and red solid symbols are for 10 mM acetate buffer.

Figure 1A shows illustrative SEC chromatograms; the relative concentration (right y axis) and normalized molecular weight profiles (left y axis) are plotted as a function of retention volume for different types of aggregation mechanisms. Each profile is an SEC chromatogram for either an unheated sample or a selected incubation time for a heated sample that illustrates different qualitative behavior in terms of SEC-MALS after a significant amount of monomer loss. The black curve (unheated sample) shows IgG1 monomer eluting as a single peak at a retention volume of approximately 8.2 mL. The blue curve illustrates the ND mechanism, which produces a mixture of dimers, trimers, and small oligomers. The green curve illustrates the CP mechanism, which is a combination of what is

observed for ND, along with high molecular weight (HMW) soluble species that elute in the exclusion volume (near 5.5 mL) and have much larger M_w values. The red curve illustrates a SEC-MALS profile when the AP growth mechanism predominates, as determined by the kinetic and mass-balance arguments below. Essentially, only monomer and HMW species are observed, although one must perform the analysis below to unambiguously conclude that AP growth is prevalent. The presence of large aggregates is not sufficient to conclude that an AP mechanism is relevant.[20,21,48,49]

The mechanisms can be distinguished qualitatively by relating M_w^{tot} to increases in the amount of monomer consumed by aggregation; $(1 - m)$ denotes the fraction of the initial monomer population that has been consumed. Previous work has shown that the relationship between M_w^{tot} and $(1 - m)^2$ depends on the relative rates of aggregate nucleation (e.g., dimerization in the present case), aggregate growth by chain polymerization or monomer addition, and growth via aggregate-aggregate coalescence or association polymerization.[20,49] One can attempt to deduce mechanisms by regressing mathematical mass-action models to time-dependent data for $m(t)$ and $M_w^{tot}(t)$, but once significant growth occurs via AP, then the quantitative fitting parameters become suspect because multiple models can fit the data equally well.[49] More generally, it has been shown that one can deduce qualitative mechanisms without a need for assuming a particular mathematical model simply by plotting $M_w^{tot}(t)$ and $[1 - m(t)]^2$ parametrically, as shown in Figure 1B−D. Each data point in Figure 1B−D corresponds to a time point from isothermal incubations at a given temperature, pH, salt concentration, and buffer type. This analysis also allows one to plot results from different solution conditions or time scales on the same scale for comparison.

The profiles in Figure 1B−D correspond to each of the representative aggregation mechanisms that were observed in 5 mM citrate solutions (blue open symbols) and 10 mM acetate solutions (red symbols). Figure 1B illustrates the ND mechanism for citrate and acetate buffer conditions. M_w^{tot}/M_0 increases essentially linearly with $(1 - m)^2$ but only reaches values less than 3 (M_0 = monomer M_w), even though the extent of monomer loss is almost 70% ($m = 0.3$ gives $(1 - m)^2 = 0.49$ on the x axis). Figure 1C illustrates aggregation through a CP mechanism. In this case, M_w^{tot} also increases linearly with $(1 - m)^2$ after an initial small nonlinear region as the first dimers are formed. For growth via CP, M_w^{tot}/M_0 continues to increase significantly beyond that for small oligomers. Figure 1D illustrates growth via AP and possibly also CP at low extents of monomer loss. That is, there is a linear scaling between M_w^{tot} and $(1 - m)^2$ at early time points (low values of $1 - m$), but then M_w^{tot} increases nonlinearly in Figure 1D at later times. The nonlinear behavior indicates growth via AP because aggregate coalescence does not consume monomer and therefore M_w^{tot}/M_0 vs $(1 - m)^2$ must curve upward because there is an increase in M_w^{tot} without a concomitant decrease in monomer concentration.[19,20,33]

The different mechanism(s) of aggregate growth are mapped in Figure 2 as aggregation state diagrams as a function of pH and ionic strength for 10 mM acetate buffer (panel A) and 5 mM citrate buffer (panel B). Each data point on the state diagram represents aggregation behavior from a time course determined through SEC-MALS analysis illustrated in Figures 1B−D. The data in Figure 2B were reported previously and confirmed separately here (data not shown).[20] The dotted lines
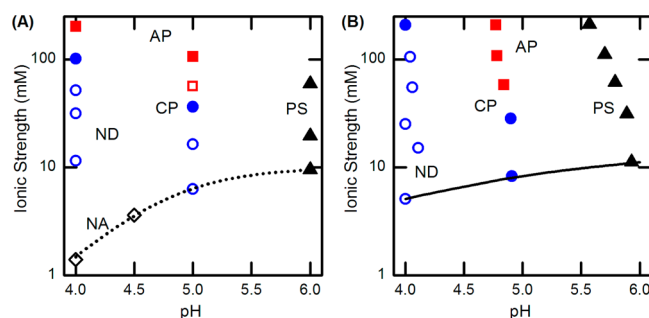

Figure 2. ASA-IgG1 aggregation state diagrams for (A) 10 mM acetate and (B) 5 mM citrate. Predominant aggregation mechanism is shown for no aggregation (open diamonds), ND (open circles), CP (filled circles), AP (filled squares), mix of CP and AP (open squares), and PS (closed triangles). The dotted curved lines illustrate the ionic strength of the (A) acetate and (B) citrate buffer component(s).

in Figure 2 show the lowest possible ionic strength that is practically achievable, given that all conditions include either 5 mM citrate or 10 mM acetate. As pH increases, the acetate or citrate ion(s) become deprotonated as one titrates the buffer with NaOH, and the net ionic strength increases because of the higher sodium and buffer anion concentrations that must result.

In terms of general trends in Figure 2, at low pH and ionic strength, the mechanism is ND, but as the pH or ionic strength increase, the mechanism shifts to CP and then AP. At higher pH and NaCl concentrations, the aggregates are ultimately insoluble and phase separate (PS). There are also a number of differences between the two state diagrams in Figure 2. One of the most pronounced is at pH 4 and low ionic strength. The acetate system exhibits no aggregation despite extreme heat treatment under those solution conditions. For example, IgG1 solutions heated at 1 mg/mL over multi-hour time scales at temperatures above T_m for this pH and ionic strength in acetate buffer did not result in detectable aggregation in SEC-MALS or by inspection (data not shown). Another pronounced difference between the acetate and citrate systems was a shift of aggregation mechanism at pH 5 and low ionic strength. The acetate system at pH 5 exhibits ND behavior, whereas aggregates grow readily via CP in citrate buffer. More subtle effects are the general shift in the boundaries between ND and CP or between CP and AP mechanisms. When moving from acetate to citrate buffer under conditions without significant added NaCl, inspection of Figure 2 shows that one typically finds that growth is less favored in acetate than in citrate.

Scaling of Aggregate Average Molecular Weight and Size by Laser Light Scattering. For aggregates that were sufficiently large to display angle-dependent scattering, the scaling of aggregate average molecular weight and size were investigated with static and quasi-elastic light scattering. SEC separates the monomer from the pool of aggregates and allows one to characterize the average aggregate molecular weight and R_g via MALS. The weight-average molecular weight of the pooled aggregate population (M_w^{agg}) was determined from SEC-MALS using the aggregate peak when it was resolvable from the monomer peak. R_g was determined as described in Methods via the angular dependence of the scattering intensity. For aggregates created under ND conditions, MALS could not be used effectively to determine reliable values because the aggregates were too small. In those cases, SAXS was measured on aggregated samples to determine the average radius of gyration using Guinier analysis (not purified with SEC). Values

for the average aggregate R_h at a given incubation time were determined from the quasi-elastic light scattering collected simultaneously with SEC-MALS as described in the Methods.

The scaling relationship between the aggregate size (characteristic dimension, R_g or R_h) and molecular weight provides insight into how mass is distributed within aggregates. Figure 3A (3B) shows power-law scaling relationships between
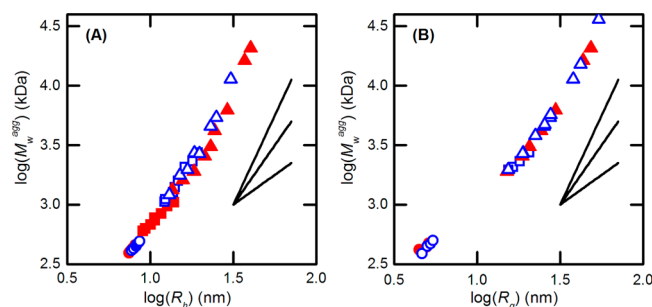

Figure 3. Scaling of average aggregate size with molecular weight based on (A) R_h or (B) R_g. ND (circles), CP (squares), and AP (triangles) depict different aggregate growth regimes. The black lines show power-law scaling relationships for slopes of 1, 2, and 3. Open blue (closed red) symbols represent aggregates created in citrate (acetate) buffer.

M_w^{agg} and R_h (R_g). Each data point corresponds to a time point for an isothermal incubation at a given temperature, pH, NaCl concentration, and buffer species. The symbols are labeled as ND (circles), CP (squares), AP (triangles), and symbol colors are labeled as blue (5 mM citrate) and red (10 mM acetate). Power-law scaling relationships with slopes of 1, 2, and 3 are also shown as straight lines in the inset of Figure 3 for reference.

Inspection of Figure 3 shows that data from different aggregation mechanisms tend to overlap with one another and fall on a common curve, which indicates the scaling regimes in Figure 3 correspond to different size regimes or degree of polymerization (M_w^{agg}/M_0) for the aggregates, rather than being dictated by the growth mechanism. The one exception is that aggregates that reached the largest sizes ($M_w \gg 10^2$ times that of monomer) did so only after AP (i.e., coalescence) became prominent, as observed previously in other systems.[20,51,52] Qualitatively, the scaling of M_w with R_g is not strictly linear and shows slight upward curvature when viewed globally across all of the values from solution conditions tested here. Within the statistical scatter in the data, it is not possible to assign separate, distinct linear regimes. Visual inspection of the data in Figure 3 indicates that the values of the local slopes for M_w vs R_g or R_h fall with the range of ~1.5 to slightly larger than 2 for smaller aggregates but the slope increase to values larger than 2 for largest aggregates. This suggests that aggregates become more compact or have a net higher fractal dimension as they become larger. However, additional details regarding the average shape of the aggregates is difficult to discern from just the scaling behavior of M_w vs R_g or R_h.[53]

Aggregate Morphology from SANS and SAXS. The average morphology of the aggregates was also characterized with small-angle neutron or X-ray scattering, SANS or SAXS, which provides a complementary technique to MALS and scaling behaviors from laser light scattering. Figure 4A (main panel) shows log−log plots of SANS scattering intensity profiles for the ND growth regime in acetate versus citrate
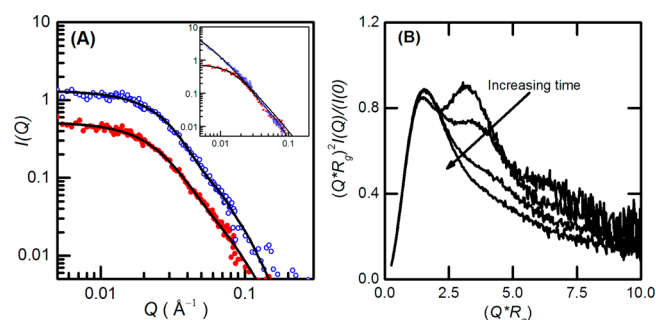

Figure 4. (A) SANS intensity profiles for purified aggregates from ND and (inset) CP growth mechanisms. Closed red symbols are shown for 10 mM acetate buffer, and open blue symbols, for 5 mM citrate. The black lines are best fits to form factor models from NCNR software. (B) Normalized SAXS Kratky plots for aggregates from ND growth mechanism. Scattering intensity was normalized to the low Q limit, and Q was normalized to the radius of gyration (cf. main text).

buffer, after purification to remove residual monomer (cf. Methods). The profiles are shown after background subtraction and normalization to the total protein concentration. The points in Figure 4A are the measured data, and the curves are best fits to geometric models for simple shapes that can be programmed analytically in available software so as to allow efficient data regression.[45] The inset of Figure 4A shows SANS profiles for aggregates created in the CP regime for acetate and citrate buffer conditions. Aggregates in the ND regime have qualitatively similar morphologies, as both conditions display relatively simple, sigmoidal profiles. Aggregates from the ND regime and CP regime (acetate) had best fits to triaxial ellipsoid form factors. Aggregates from the CP regime (citrate) and AP regime (shown in Supporting Information) had best fits to a fractal with flexible cylinder subunits. Details on the fitting parameters are provided in the Supporting Information.

Figure 4B illustrates SAXS results, which are presented as normalized Kratky plots for the ND mechanism. Each curve is a quenched sample from an isothermal incubation at the temperature(s) used to generate the data in Figures 1C. SAXS Kratky plots for different isothermal time points were compared by normalizing the intensity $I(Q)$ to the low Q intensity $I(Q=0)$, and scaling Q by the R_g value for a given sample based on the Guinier analysis. $I(Q)$ curves plateau at low Q because the aggregates do not grow to be large in the ND mechanism, and the plateau corresponds to the weight average molecular weight of the sample. As noted elsewhere, scaling the SAXS data in this way allows one to normalize SAXS Kratky plots by size and molecular weight and compare differences in morphology.[54] The curve for IgG1 monomer in Figure 4B has two peaks; one at $Q*R_g = 1.5$, which corresponds to a length scale similar to the ensemble averaged size, and another peak at $Q*R_g = 3.1$, which corresponds to length scales smaller than the average size. The secondary peak at these shorter length scales has previously been attributed to correlations in the positions of the Fc and Fab domains due to the flexibility in the hinge region of the native IgG1.[55,56]

As aggregation proceeds, the left-most peak in Figure 4B increases and shifts to slightly larger $Q*R_g$ (~ 1.55). Interestingly, aggregated samples for different time points all have the same location of the peak maximum when plotted versus $Q*R_g$, regardless of the amount of monomer remaining or how much aggregate growth has occurred. This suggests the average aggregate morphology from the ND regime is compact
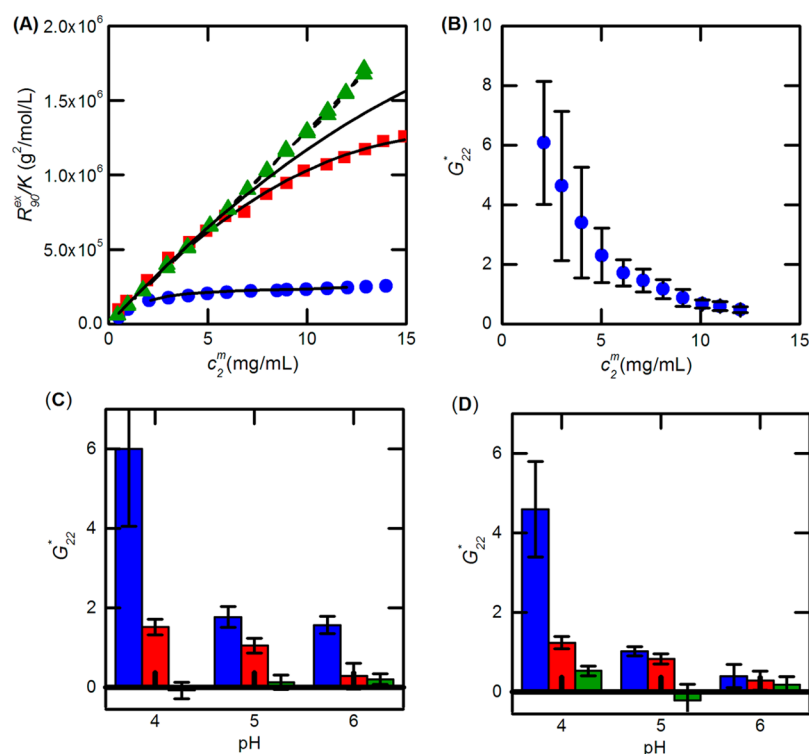
Figure 5. (A) Excess Rayleigh ratio vs IgG1 concentration for pH 4, 10 mM acetate with 0 mM NaCl (circles), 20 mM NaCl (squares), and 200 mM NaCl (triangles). Colored curves are fits to eq 2, and the black curve is the Rayleigh ratio for a hard sphere with equivalent diameter to the IgG1. (B) G_{22}^* values determined as a function of protein concentration for pH 4, 0 mM NaCl, 10 mM acetate. At other pH and NaCl concentrations, G_{22} is not a function of concentration in the range of protein concentration tested. G_{22}^* values are shown for (C) 10 mM acetate and (D) 5 mM citrate buffer, for 0 mM NaCl (blue), 20 mM NaCl (red), and 200 mM NaCl (green). Error bars represent 95% confidence intervals.

and remains qualitatively similar, regardless of how the aggregates are distributed among dimer, trimer, tetramer, etc.

Protein−Protein Interactions Based on Static Light Scattering. Average protein−protein interactions for AS-IgG1 monomer were investigated using static light scattering and Kirkwood−Buff analysis. Illustrative results for the excess Rayleigh ratio as a function of protein concentration are given in Figure 5A. The Kirkwood−Buff integral for protein−protein interactions, G_{22}, was determined using linear regression to eq 2 when a single value of G_{22} provided a good description of the data. When G_{22} changed appreciably with protein concentration, a sliding-window method was instead more appropriate. Illustrative results are provided as Figure 5B, with details of the regression method provided elsewhere.[57]

Physically, G_{22} provides a measure of net attractions or repulsions between IgG1 molecules in the solution, averaged over all neighboring proteins around a given central protein. It includes simultaneous contributions from multiple neighboring proteins, and as such, it is a valid and rigorously defined measure of protein−protein interactions in both dilute and concentrated solutions and for both weak and strong protein−protein interactions.[37] G_{22} was determined at pH 4, 5, and 6 with the addition of 0, 20, and 200 mM NaCl concentrations in 5 mM citrate buffer and in 10 mM acetate buffer. Salt concentrations were chosen to provide a range of Debye−Hückel screening lengths within the same ranges as those for the aggregation state diagrams in Figure 2. The values of G_{22} are normalized by the value of B_{22} that corresponds to hard sphere or steric-only interactions, denoted B_{22}^{HS}, as suggested by previous theoretical arguments.[58] The reduced or normalized

G_{22} is defined as $G_{22}^* = -G_{22}/2B_{22}^{HS}$). Using this definition, positive values of G_{22}^* correspond to net repulsive protein−protein interactions relative to an ideal (noninteracting) system, and vice versa for negative values. A G_{22} value of unity is expected for purely steric repulsions at low protein concentrations.

Figure 5C,D shows G_{22}^* values measured in 10 mM acetate buffer and 5 mM citrate, respectively. The pI of this IgG1 is ∼9, and the molecule is expected to have a net positive charge under all solution conditions tested here. As pH is decreased farther away from the pI, the net charge on the protein surface will increase and lead to larger electrostatic repulsions, consistent with the results shown in Figure 5. With the addition of 200 mM NaCl, charge screening might expected to be sufficient to minimize electrostatic repulsions between protein molecules. The results in Figure 5 show that G_{22}^* does not become significantly less than zero, but it is less than one, with the addition of 200 mM NaCl. This suggests weak attractive non-electrostatic interactions are present, even if electrostatic repulsions are not completely screened by 200 mM NaCl.

Protein Charge Determined by Electrophoretic Light Scattering (ELS). IgG1 net charge (valence) was inferred from electrophoretic mobility measurements as a function of pH, NaCl concentration, and buffer species using electrophoretic light scattering. Electrophoretic mobility was determined by measuring the IgG1 velocity in solution under the influence of a steady electric field, as a function of electric field strength, and the friction coefficient or protein diffusion coefficient was determined from QELS (cf. Methods). These quantities were combined to give values for Z_{eff} via eq 7.

Figure 6A,B shows Z_{eff} of monomer IgG1 as a function of pH and added NaCl concentration, based on fits of electrophoretic
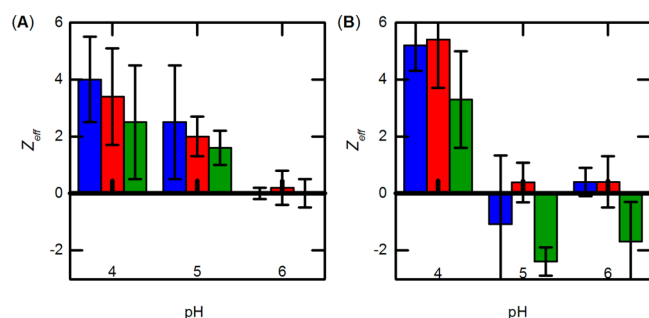

Figure 6. Net effective charge from ELS analysis for 10 mM acetate (A) and 5 mM citrate (B) for 20 mM NaCl (blue), 40 mM NaCl (red), and 100 mM NaCl (green). Error bars are 95% confidence intervals.

velocity vs electric field strength (shown in Supporting Information). Panel A (B) corresponds to acetate (citrate) buffer conditions. In all cases, PEG was used as a neutral control to detect electro-osmotic flow (EOF). Measurable EOF was only observed at pH 6 in 5 mM citrate conditions and was corrected for, as described in the Methods.

Given the inherently large statistical uncertainties in the measured Z_{eff} values, only qualitative trends can be drawn with confidence from the results in Figure 6. For both buffer types, the net charge was positive at pH 4 but was statistically indistinguishable as a function of NaCl concentration. At pH 5 in acetate buffer, the net charge was positive. However, at pH 5 in citrate buffer, the net charge was statistically insignificant from zero; except at high NaCl concentration, where the data were consistent with charge inversion due to anion binding. The much lower net charge at pH 5 with citrate might be a result of preferential accumulation of the divalent citrate anions at the protein surface. Table 1 reports calculated concentrations

Table 1. Buffer Anions Concentration as a Function of pH[a]

buffer anions	pH 4	pH 5	pH 6
$C_2H_3O_2^-$ (mM)	1.5	6.4	9.5
$C_6H_7O_7^-$ (mM)	3.8	1.8	0.19
$C_6H_6O_7^{2-}$ (mM)	0.66	3.1	3.4
$C_6H_5O_2^{3-}$ (mM)	0.0026	0.12	1.4

[a]Concentration of acetate ion is the first row followed by citrate ions.

of the different buffer anion species in solution at pH 4, 5, and 6 based on $pK_a(s)$ of acetate and citrate,[59] illustrating the shift from predominantly monovalent anions for citrate at low pH, to divalent and trivalent anions at higher pH conditions. While preferential accumulation of multivalent citrate anions may also be anticipated at pH 6 due to both divalent and trivalent anions, this may be too weak of an affect to be apparent experimentally if the shift to pH 6 causes the inherent surface charge on the protein to be greatly reduced.

■ DISCUSSION

As Figures 1 and 2 illustrate, aggregation of ASA-IgG1 proceeds via different pathways that depend on the solution conditions. Depending on the pH, NaCl concentration, and identity of the buffer species, different mechanisms predominate. In all cases, the aggregates were effectively irreversible, as no aggregate

dissociation was observed upon dilution or upon standing over multiday time scales for any of the conditions tested. The solution conditions effectively dictated whether aggregates (i) would remain small (i.e., ND, meaning minimal growth of aggregates), (ii) would grow by CP or by AP to create much larger soluble, aggregates, (iii) or would effectively phase separate (PS) as macroscopic particles that sediment easily on the bench or under mild centrifugation.

As pH increases toward the pI, the IgG1 surface charge decreases. The pH will also affect the concentration of different buffer ions in solution. The solution ionic strength will be affected by the buffer pK_a value(s) and the addition of NaCl (0–200 mM in the present work). At a mean-field level, ions in solution create a Debye double layer, which screens the electrostatic repulsions felt between IgG1 monomers as well as repulsions between monomers and aggregates and those between aggregates.

Figure 7A schematically illustrates the effect of pH and ionic strength on a hypothetical potential of mean force, W, felt by
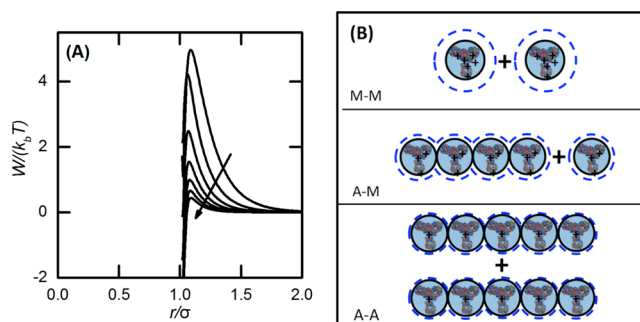

Figure 7. Schematic depiction of electrostatic colloidal interactions causing shifts in observed aggregation mechanisms. (A) Potential mean force W/k_BT plotted as a function of center-to-center distance for two hard spheres with the same hydrodynamic radius as an IgG1. The blue arrow shows the effect of decreasing $|Z_{eff}|$ (changing pH toward the pI) and increasing ionic strength (increasing NaCl concentration). (B) Schematic describing monomer−monomer (M−M), monomer−aggregate (M−A), and aggregate−aggregate (A−A) association (cf. main text).

two IgG1 molecules. W/k_BT, is plotted versus the center-to-center distance scaled by the effective diameter of IgG1 monomer, r/σ. For illustration, the electrostatic interactions between IgG1 molecules are described simply using a screened Coulomb potential.[60] Z_{eff} values based on a multivariate fit to the experimental values in Figure 6 were input into the colloidal model along with screening lengths calculated using Debye−Hückel theory and the relevant ionic strength.

The arrow indicates the shifts in W/k_BT for increasing pH and NaCl concentration. As the value of Z_{eff} is reduced with increasing pH and/or the screening length decreases with increasing ionic strength, the electrostatic repulsions felt between two proteins decrease. While the W/k_BT profiles in Figure 7A are for two IgG1 interacting monomers, analogous profiles could be created for an IgG1 monomer interacting with an aggregate or for interactions between two aggregates. In these latter cases, the aggregate geometry will affect the energy barriers, as illustrated below.

Figure 7B depicts other scenarios for association of different species using simplified geometries to qualitatively illustrate each aggregate growth mechanism (ND, CP, and AP). In each case, two species (monomer or aggregate) come together as

part of the process to form a larger species. IgG monomers are shown simply with black circles, and when circles are touching it denotes an aggregate that has more than one constituent monomer. The blue dotted circle traced around each black circle represents the thickness of the Debye double layer. Pairs are shown as monomer−monomer (M−M), monomer−aggregate (M−A) in an end-to-end orientation, and aggregate−aggregate (A−A) in the same plane with a side-to-side orientation.

M−M association is the dominant aggregation event for the ND growth regime observed at low pH and ionic strength. The protein surface has large positive charge, which is represented pictorially as a series of positive signs on the IgG1 surface. At low ionic strength, the Debye double layer extends well beyond the protein surface. Under these solution conditions, the electrostatic contributions to the potential mean force for M−M interactions will be strongly repulsive. Colloidal interaction for other geometries (M−A and A−A) would have even larger repulsive forces because as M approaches A or A approaches another A, repulsions will be felt simultaneously by multiple constituent proteins within an aggregate. As a result, growth beyond small aggregates (e.g., dimers, trimers) is greatly disfavored.

As the pH and ionic strength are increased, association between species presumably becomes more favorable because the protein surface charge will be decreased, and the Debye double layer thickness will decrease with addition of ionized buffer species. As a result, M−A association becomes more viable from a kinetic perspective, as the repulsive interactions have decreased. Aggregate−aggregate association (A−A) will also become more viable at higher pH and ionic strength. At a pH value approaching the pI and/or at elevated ionic strength, M−M and M−A interactions will also be expected to have insignificant electrostatic energy barriers and therefore all mechanisms will occur simultaneously.

These simple geometries and colloidal arguments based on the potential of mean force are consistent with the qualitative and semiquantitative behavior of the aggregation state diagrams in Figure 2. However, one needs to bear in mind that aggregation is a multistep pathway with many possible rate-determining steps. As shown in Figure 3 and as discussed below, the scaling behavior for average molecular weight and size of aggregates appears to depend primarily on size (i.e., extent of polymerization). The results suggest that electrostatic interactions cause changes in the relative rates of the different growth mechanisms, rather than the morphology of the resulting aggregates. The colloidal arguments above can only explain energy barriers smaller than $\sim 10 k_B T$. One needs to include noncolloidal factors, such as aggregation-prone regions or hotspots that are specific to particular sequences in the protein,[61] if one is to explain why monomers aggregate despite such large barriers.[20,62] Another limitation of the colloidal model is that it cannot explain specific-ion effects observed in the aggregation mechanism at low the NaCl concentration. If an anion preferentially accumulates, such as citrate, then the Debye double layer will effectively be shorter than what mean-field arguments would predict, and this would result in greater screening of electrostatic repulsions. Higher buffer concentrations were not explored systematically in the present work, but one might anticipate that citrate and acetate would display specific-ion effects that are beyond mean-field ionic strength arguments under those conditions.

Additional considerations include chemical stability (e.g., fragmentation, deamidation, oxidation) that might be anticipated to produce protein species that are more or less prone to aggregate. This is especially the case when one considers colder temperatures where aggregation rates are much slower, and chemical degradation rates may easily compete with those for aggregation.[2] Chemical stability of AS-IgG1 was not tested as part of the present work, and will need to be included in future work to address such considerations.

A combination of laser light scattering, SAXS, and SANS was used to characterize aggregate morphology for each mechanism. Using the power-law scaling relationship between the aggregate molecular weight and radius of gyration one can gain insight into how the mass is distributed around the aggregate center of mass. The exponent in eq 9 is defined as the fractal dimension.[53]

$$M_w^{agg} \sim R_g^{\,d_f} \tag{9}$$

Illustrative values of the fractal dimensions for a simple objects include $d_f = 1$ for a long rod, $d_f = 1.86$ for diffusion-limited colloidal aggregates (DLCA),[63] $d_f = 2$ for flat disks, $d_f = 2.1$ for reaction-limited colloidal aggregates (RLCA),[64] and $d_f = 3$ for uniform spheres. As the fractal dimension increases, the mass becomes more uniformly distributed around the object's center of mass. The concept of a fractal is best applied for large disordered architectures with self-similarities where the subunit is much smaller than the overall object.[65] Fractal behavior occurs for small aggregates, but the fractal concept works well for aggregates composed of 20 subunits and is a reasonable for even smaller aggregates.[66]

In the present case, Figure 3 shows that d_f increases as the aggregates become larger. The value of d_f appears to primarily be determined by the size (or molecular weight) of the aggregates rather than the solution conditions or presence of citrate versus acetate anions. However, once one considers that larger aggregates may have multiple branch points that would lead to a higher d_f but with aggregate shapes that are highly nonuniform, it becomes clear that one should not interpret the scaling results as being more than qualitative or semi-quantitative in the present context. The measured SANS and SAXS profiles do not provide a means to further differentiate morphologies, but they are qualitatively consistent with the results from MALS. For dimers and similarly small aggregates, it is difficult to define how compact or extended they are in terms of a value for d_f based on Figure 3. However, the SAXS and SANS data are consistent with dimers being more globular than the folded IgG. As aggregates grow to intermediate sizes by CP or AP, they adopt relatively low fractal dimension structures ($d_f \sim 2$ in Figure 3). The upward curvature in Figure 3 shows that aggregates become somewhat more compact (higher d_f) at the largest sizes. Preliminary results from cryotransmission electron microscopy (not shown) are qualitatively consistent with higher fractal-dimension structures for larger aggregates. More quantitative structural conclusions are difficult to justify because of known limitations with scattering-based techniques, including bias toward scattering by large objects, and the fact that aggregate growth necessarily increases the polydispersity of the aggregate population.[49]

Finally, one must bear in mind that aggregate nucleation and growth by addition of monomers both require some degree of unfolding to allow aggregation-prone hotspots to be exposed. This necessarily means that there are only a select number of

geometric ways that proteins can form strong connections with one another as they form aggregates of different sizes. As such, one might anticipate that aggregates formed through different mechanisms (e.g., CP vs AP) should have significantly different d_f values. The present data do not provide a clear assessment of this hypothesis. This is due, at least in part, to the fact that CP and AP mechanisms occur simultaneously, just with different net rates. As such, many of the state points and time points upon which Figures 3 and 4 are based likely include aggregates from both mechanisms.

Finally, we consider whether G_{22}^* is semiquantitatively predictive for which AS-IgG1 aggregation mechanisms predominate for a given solution condition. G_{22} is a measure of net PPI, including repulsions due to screened electrostatic and steric interactions and any electrostatic and nonelectrostatic attractions. G_{22} is rigorously related to the integral over the potential of mean force between proteins, and determination of its experimental value does not require one to assume an underlying model for those interactions or extrapolate from a narrow set of solution conditions.[36,57] The potential of mean force, $W_{22}(r)$, integrated over the intermolecular center to center distance, r, can be related to G_{22}, as shown in eq 10.[37] However, unlike what was used in Figure 7, W_{22} can have multibody contributions that are not accounted for by dilute-solution treatments.

$$G_{22} = \int_{\infty}^{0} (e^{-W_{22}(r)/k_B T} - 1) 4\pi r^2 \, dr \tag{10}$$

In the arguments above regarding the simple colloidal model for why the state diagrams have the qualitative features that are observed, no nonidealities were accounted for in the protein–protein interactions beyond those based on mean-field colloidal arguments (e.g., net charge and screening lengths compared to protein dimensions). However, G_{22} values (Figure 5) clearly show that there are differences in protein–protein interactions when one considers the acetate and citrate systems at lower NaCl concentrations. While the colloidal model above illustrate the role of electrostatic protein–protein interaction, it fails to capture specific-ion effects. However, the measured values for G_{22} do not suffer from this limitation.

A multivariate surface was fit to experimental G_{22}^* values determined from SLS (additional details, including fitted coefficients and p-values, are provided in Supporting Information). Figure 8 superimposes the G_{22}^* response surfaces as a function of pH and ionic strength with the corresponding aggregation state diagrams for acetate (panel A) and citrate
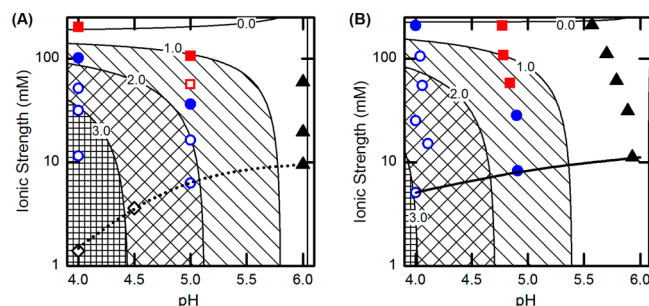
(panel B) conditions. G_{22}^* correlates semiquantitatively with the aggregation mechanism in citrate vs acetate. When net repulsions are sufficiently large, aggregation proceeds through ND (G_{22}^* between approximately 2 and 3 for both acetate and citrate systems). As G_{22}^* decreases with increasing pH and ionic strength, the aggregation mechanism shifts to CP. G_{22}^* values of ~1 to 2 correspond to CP growth and transitioning to AP growth. Finally, aggregation occurs via AP and PS as G_{22}^* shifts to values less than unity, i.e., when electrostatic repulsions are not sufficient to outweigh (nonelectrostatic) attractions. Overall, G_{22}^* appears to be a reasonable predictor of IgG1's aggregation mechanism. While only phenomenological, it offers an experimental measure of net protein–protein interactions, which inherently captures specific-ion effects and does not rely on model regression or simplifying model assumptions.

SUMMARY AND CONCLUSIONS

Changing the buffer from citrate to acetate had significant effects with respect to shifting the aggregation mechanism(s) or state diagrams and altering protein–protein interactions for AS-IgG1 as a function of solution conditions (pH, [NaCl]) that are typical for therapeutic proteins to experience during purification, drug product manufacturing, and final product storage. Shifts for the scaling of aggregate average molecular weight and size appeared to be determined primarily by the size of the aggregates rather than aggregate mechanism or protein–protein interactions. Simple models qualitatively illustrate how changes in electrostatic repulsions can explain the features of state diagrams and suggest that preferential interactions of proteins with ions can also alter rates of competing aggregation pathways. Those same models cannot predict specific-ion effects such as the difference between citrate and acetate for the AS-IgG1 system. Independent of the ability to predict specific-ion effects, experimental G_{22}^* values may offer a phenomenological, semiquantitative means to predict which aggregate growth mechanism(s) will predominate.

ASSOCIATED CONTENT

Ⓢ Supporting Information

Detailed information including incubation temperatures and DSC peak temperature, SANS model fitting parameters, details related to the electrophoretic mobility measurements, and results for the statistical analysis for G_{22}^* surface. Additionally, more in depth analysis of normalized Kratky plots are also reported. The Supporting Information is available free of charge on the ACS Publications website at DOI: 10.1021/acs.jpcb.5b01881.

AUTHOR INFORMATION

Corresponding Author
*Tel.: 302-831-0838; Fax: 302-831-1048; E-mail: cjr@udel.edu.

Notes
The authors declare no competing financial interest.

Figure 8. Overlay of the IgG1 aggregation state diagrams with G_{22}^* surfaces from multivariate regression for (A) 10 mM acetate and (B) 5 mM citrate. Labels are G_{22}^* values determine from the multivariate regression. Symbols have the same meaning as those in Figure 2.

conducted at the Cornell High Energy Synchrotron Source (CHESS), which is supported by the National Science Foundation (award DMR-0936384), using the Macromolecular Diffraction at CHESS (MacCHESS) facility, which is supported by award GM-103485 from the National Institutes of Health, through its National Institute of General Medical Sciences. Certain commercial equipment, instruments, or materials (or suppliers, or software) are identified in this article to foster understanding. Such identification implies neither recommendation or endorsement by the National Institute of Standards and Technology nor that the materials or equipment identified are necessarily the best available for the purpose.

■ REFERENCES

(1) Aggarwal, S. R. What's Fueling the Biotech Engine—2012 to 2013. *Nature* **2014**, *201*, 4.

(2) *Aggregation of Therapeutic Proteins*, 1 ed.; Wang, W., Roberts, C. J., Eds.; Wiley: Hoboken, NJ, 2011.

(3) Boehm, M. K.; Woof, J. M.; Kerr, M. A.; Perkins, S. J. The Fab and Fc Fragments of IgA1 Exhibit a Different Arrangement from That in IgG: A Study by X-Ray and Neutron Solution Scattering and Homology Modelling. *J. Mol. Biol.* **1999**, *286*, 1421−1447.

(4) Vlasak, J.; Ionescu, R. Fragmentation of Monoclonal Antibodies. *mAbs* **2011**, *3*, 253−263.

(5) Liu, D.; Ren, D.; Huang, H.; Dankberg, J.; Rosenfeld, R.; Cocco, M. J.; Li, L.; Brems, D. N.; Remmele, R. L. Structure and Stability Changes of Human IgG1 Fc as a Consequence of Methionine Oxidation. *Biochemistry (Moscow)* **2008**, *47*, 5088−5100.

(6) Yi, L.; Beckley, N.; Gikanga, B.; Zhang, J.; Wang, Y. J.; Chih, H.-W.; Sharma, V. K. Isomerization of Asp-Asp Motif in Model Peptides and a Monoclonal Antibody Fab Fragment. *J. Pharm. Sci.* **2013**, *102*, 947−959.

(7) Cromwell, M. E.; Hilario, E.; Jacobson, F. Protein Aggregation and Bioprocessing. *AAPS J.* **2006**, *8*, E572−E579.

(8) Vázquez-Rey, M.; Lang, D. A. Aggregates in Monoclonal Antibody Manufacturing Processes. *Biotechnol. Bioeng.* **2011**, *108*, 1494−1508.

(9) Wang, W.; Singh, S. K.; Li, N.; Toler, M. R.; King, K. R.; Nema, S. Immunogenicity of Protein aggregates—Concerns and Realities. *Int. J. Pharm.* **2012**, *431*, 1−11.

(10) Carpenter, J. F.; Randolph, T. W.; Jiskoot, W.; Crommelin, D. J. A.; Middaugh, C. R.; Winter, G.; Fan, Y.-X.; Kirshner, S.; Verthelyi, D.; Kozlowski, S.; et al. Overlooking Subvisible Particles in Therapeutic Protein Products: Gaps That May Compromise Product Quality. *J. Pharm. Sci.* **2009**, *98*, 1201−1205.

(11) Rosenberg, A. S. Effects of Protein Aggregates: An Immunologic Perspective. *AAPS J.* **2006**, *8*, E501−E507.

(12) Hansel, T. T.; Kropshofer, H.; Singer, T.; Mitchell, J. A.; George, A. J. T. The Safety and Side Effects of Monoclonal Antibodies. *Nat. Rev. Drug Discovery* **2010**, *9*, 325−338.

(13) Baker, M. P.; Reynolds, H. M.; Lumicisi, B.; Bryson, C. J. Immunogenicity of Protein Therapeutics. *Self Nonself* **2010**, *1*, 314−322.

(14) Sethu, S.; Govindappa, K.; Alhaidari, M.; Pirmohamed, M.; Park, K.; Sathish, J. Immunogenicity to Biologics: Mechanisms, Prediction and Reduction. *Arch. Immunol. Ther. Exp.* **2012**, *60*, 331−344.

(15) Kumar, S.; Mitchell, M. A.; Rup, B.; Singh, S. K. Relationship between Potential Aggregation-Prone Regions and HLA-DR-Binding T-Cell Immune Epitopes: Implications for Rational Design of Novel and Follow-On Therapeutic Antibodies. *J. Pharm. Sci.* **2012**, *101*, 2686−2701.

(16) Brummitt, R. K.; Nesta, D. P.; Chang, L.; Chase, S. F.; Laue, T. M.; Roberts, C. J. Nonnative Aggregation of an IgG1 Antibody in Acidic Conditions: Part 1. Unfolding, Colloidal Interactions, and Formation of High-Molecular-Weight Aggregates. *J. Pharm. Sci.* **2011**, *100*, 2087−2103.

(17) Hari, S. B.; Lau, H.; Razinkov, V. I.; Chen, S.; Latypov, R. F. Acid-Induced Aggregation of Human Monoclonal IgG1 and IgG2:

(18) Latypov, R. F.; Hogan, S.; Lau, H.; Gadgil, H.; Liu, D. Elucidation of Acid-Induced Unfolding and Aggregation of Human Immunoglobulin IgG1 and IgG2 Fc. *J. Biol. Chem.* **2012**, *287*, 1381−1396.

(19) Weiss, W. F.; Young, T. M.; Roberts, C. J. Principles, Approaches, and Challenges for Predicting Protein Aggregation Rates and Shelf Life. *J. Pharm. Sci.* **2009**, *98*, 1246−1277.

(20) Kim, N.; Remmele, R. L.; Liu, D.; Razinkov, V. I.; Fernandez, E. J.; Roberts, C. J. Aggregation of Anti-streptavidin Immunoglobulin Gamma-1 Involves Fab Unfolding and Competing Growth Pathways Mediated by pH and Salt Concentration. *Biophys. Chem.* **2013**, *172*, 26−36.

(21) Li, Y.; Ogunnaike, B. A.; Roberts, C. J. Multi-variate Approach to Global Protein Aggregation Behavior and Kinetics: Effects of pH, NaCl, and Temperature for α-Chymotrypsinogen A. *J. Pharm. Sci.* **2009**, *99*, 645−662.

(22) Andrews, J. M.; Weiss; Roberts, C. J. Nucleation, Growth, and Activation Energies for Seeded and Unseeded Aggregation of α-Chymotrypsinogen A. *Biochemistry (Moscow)* **2008**, *47*, 2397−2403.

(23) Weijers, M.; Broersen, K.; Barneveld, P. A.; Cohen Stuart, M. A.; Hamer, R. J.; De Jongh, H. H. J.; Visschers, R. W. Net Charge Affects Morphology and Visual Properties of Ovalbumin Aggregates. *Biomacromolecules* **2008**, *9*, 3165−3172.

(24) Narhi, L. O.; Schmit, J.; Bechtold-Peters, K.; Sharma, D. Classification of Protein Aggregates. *J. Pharm. Sci.* **2012**, *101*, 493−498.

(25) Zhang-van Enk, J.; Mason, B. D.; Yu, L.; Zhang, L.; Hamouda, W.; Huang, G.; Liu, D.; Remmele, R. L.; Zhang, J. Perturbation of Thermal Unfolding and Aggregation of Human IgG1 Fc Fragment by Hofmeister Anions. *Mol. Pharmaceutics* **2013**, *10*, 619−630.

(26) Arosio, P.; Jaquet, B.; Wu, H.; Morbidelli, M. On the Role of Salt Type and Concentration on the Stability Behavior of a Monoclonal Antibody Solution. *Biophys. Chem.* **2012**, *168−169*, 19−27.

(27) Kroetsch, A. M.; Sahin, E.; Wang, H.; Krizman, S.; Roberts, C. J. Relating Particle Formation to Salt- and pH-Dependent Phase Separation of Non-Native Aggregates of Alpha-Chymotrypsinogen A. *J. Pharm. Sci.* **2012**, *101*, 3651−3660.

(28) Schneider, C. P.; Shukla, D.; Trout, B. L. Arginine and the Hofmeister Series: The Role of Ion−Ion Interactions in Protein Aggregation Suppression. *J. Phys. Chem. B* **2011**, *115*, 7447−7458.

(29) Baldwin, R. L. How Hofmeister Ion Interactions Affect Protein Stability. *Biophys. J.* **1996**, *71*, 2056−2063.

(30) Rubin, J.; Linden, L.; Coco, W. M.; Bommarius, A. S.; Behrens, S. H. Salt-Induced Aggregation of a Monoclonal Human Immunoglobulin G1. *J. Pharm. Sci.* **2013**, *102*, 377−386.

(31) Gokarn, Y. R.; Fesinmeyer, R. M.; Saluja, A.; Razinkov, V.; Chase, S. F.; Laue, T. M.; Brems, D. N. Effective Charge Measurements Reveal Selective and Preferential Accumulation of Anions, but Not Cations, at the Protein Surface in Dilute Salt Solutions: Effective Charge Measurements Reveal Direct Anion−Protein Interactions. *Protein Sci.* **2011**, *20*, 580−587.

(32) Sahin, E.; Grillo, A. O.; Perkins, M. D.; Roberts, C. J. Comparative Effects of pH and Ionic Strength on Protein−Protein Interactions, Unfolding, and Aggregation for IgG1 Antibodies. *J. Pharm. Sci.* **2010**, *99*, 4830−4848.

(33) Sahin, E.; Roberts, C. J. Size-Exclusion Chromatography with Multi-angle Light Scattering for Elucidating Protein Aggregation Mechanisms. *Methods Mol. Biol.* **2012**, *899*, 403−423.

(34) Yearley, E. J.; Zarraga, I. E.; Shire, S. J.; Scherer, T. M.; Gokarn, Y.; Wagner, N. J.; Liu, Y. Small-Angle Neutron Scattering Characterization of Monoclonal Antibody Conformations and Interactions at High Concentrations. *Biophys. J.* **2013**, *105*, 720−731.

(35) *ASTRA VI*; Wyatt Technology Corporation: Santana Barbara, CA, 2012.

(36) Blanco, M. A.; Sahin, E.; Li, Y.; Roberts, C. J. Reexamining Protein−Protein and Protein−Solvent Interactions from Kirkwood−

Buff Analysis of Light Scattering in Multi-component Solutions. *J. Chem. Phys.* **2011**, *134*, 225103.

(37) Ben-Naim, A. *Statistical Thermodynamics for Chemists and Biochemists*; Springer: New York, 2013.

(38) Nielsen, S. S.; Toft, K. N.; Snakenborg, D.; Jeppesen, M. G.; Jacobsen, J. K.; Vestergaard, B.; Kutter, J. P.; Arleth, L. *BioXTAS RAW, a Software Program for High-Throughput Automated Small-Angle X-ray Scattering Data Reduction and Preliminary Analysis. J. Appl. Crystallogr.* **2009**, *42*, 959−964.

(39) Frisken, B. J. Revisiting the Method of Cumulants for the Analysis of Dynamic Light-Scattering Data. *Appl. Opt.* **2001**, *40*, 4087−4091.

(40) Koppel, D. E. Analysis of Macromolecular Polydispersity in Intensity Correlation Spectroscopy: The Method of Cumulants. *J. Chem. Phys.* **1972**, *57*, 4814−4820.

(41) Corbett, J. C. W.; Connah, M. T.; Mattison, K. Advances in the Measurement of Protein Mobility Using Laser Doppler Electro-phoresis—the Diffusion Barrier Technique. *Electrophoresis* **2011**, *32*, 1787−1794.

(42) Gimsa, J.; Eppmann, P.; Prüger, B. Introducing Phase Analysis Light Scattering for Dielectric Characterization: Measurement of Traveling-Wave Pumping. *Biophys. J.* **1997**, *73*, 3309−3316.

(43) John, F; Miller, K. S. The Determination of Very Small Electrophoretic Mobilities in Polar and Nonpolar Colloidal Dispersions Using Phase Analysis Light Scattering. *J. Colloid Interface Sci.* **1991**, 532−554.

(44) Durant, J. A.; Chen, C.; Laue, T. M.; Moody, T. P.; Allison, S. A. Use of T4 Lysozyme Charge Mutants to Examine Electrophoretic Models. *Biophys. Chem.* **2002**, *101*, 593−609.

(45) Kline, S. R. Reduction and Analysis of SANS and USANS Data Using IGOR Pro. *J. Appl. Crystallogr.* **2006**, *39*, 895−900.

(46) Covington, A. K.; Paabo, M.; Robinson, R. A.; Bates, R. G. Use of the Glass Electrode in Deuterium Oxide and the Relation between the Standardized pD (paD) Scale and the Operational pH in Heavy Water. *Anal. Chem.* **1968**, *40*, 700−706.

(47) *Neutron, X-Rays and Light. Scattering Methods Applied to Soft Condensed Matter*, 1 ed.; Zemb, T., Lindner, P., Eds.; North Holland: Amsterdam, 2002.

(48) Brummitt, R. K.; Nesta, D. P.; Roberts, C. J. Predicting Accelerated Aggregation Rates for Monoclonal Antibody Formulations, and Challenges for Low-Temperature Predictions. *J. Pharm. Sci.* **2011**, *100*, 4234−4243.

(49) Li, Y.; Roberts, C. J. Lumry−Eyring Nucleated-Polymerization Model of Protein Aggregation Kinetics. 2. Competing Growth via Condensation and Chain Polymerization. *J. Phys. Chem. B* **2009**, *113*, 7020−7032.

(50) Roberts, C. J.; Das, T. K.; Sahin, E. Predicting Solution Aggregation Rates for Therapeutic Proteins: Approaches and Challenges. *Int. J. Pharm.* **2011**, *418*, 318−333.

(51) Arosio, P.; Rima, S.; Lattuada, M.; Morbidelli, M. Population Balance Modeling of Antibodies Aggregation Kinetics. *J. Phys. Chem. B* **2012**, *116*, 7066−7075.

(52) Feder, J.; Jøssang, T.; Rosenqvist, E. Scaling Behavior and Cluster Fractal Dimension Determined by Light Scattering from Aggregating Proteins. *Phys. Rev. Lett.* **1984**, *53*, 1403−1406.

(53) Burchard, W. Solution Properties of Branched Macromolecules. In *Branched Polymers II*; Roovers, J., Ed.; Springer: Berlin, 1999; pp 113−194.

(54) Receveur-Bréchot, V.; Durand, D. How Random Are Intrinsically Disordered Proteins? A Small Angle Scattering Perspective. *Curr. Protein Pept. Sci.* **2012**, *13*, 55.

(55) Clark, N. J.; Zhang, H.; Krueger, S.; Lee, H. J.; Ketchem, R. R.; Kerwin, B.; Kanapuram, S. R.; Treuheit, M. J.; McAuley, A.; Curtis, J. E. Small-Angle Neutron Scattering Study of a Monoclonal Antibody Using Free-Energy Constraints. *J. Phys. Chem. B* **2013**, *117*, 14029−14038.

(56) Ashish; Solanki, A. K.; Boone, C. D.; Krueger, J. K. Global Structure of HIV-1 Neutralizing Antibody IgG1 b12 Is Asymmetric. *Biochem. Biophys. Res. Commun.* **2010**, *391*, 947−951.

(57) Blanco, M. A.; Perevozchikova, T.; Martorana, V.; Manno, M.; Roberts, C. J. Protein−Protein Interactions in Dilute to Concentrated Solutions: α-Chymotrypsinogen in Acidic Conditions. *J. Phys. Chem. B* **2014**, *118*, 5817−5831.

(58) Grünberger, A.; Lai, P.-K.; Blanco, M. A.; Roberts, C. J. Coarse-Grained Modeling of Protein Second Osmotic Virial Coefficients: Sterics and Short-Ranged Attractions. *J. Phys. Chem. B* **2013**, *117*, 763−770.

(59) Stoll, V. S.; Blanchard, J. S. Buffers. In *Methods in Enzymology*; Elsevier: Amsterdam, 2009; Chapter 6, Vol. *463*, pp 43−56.

(60) Hayter, J. B.; Penfold, J. An Analytic Structure Factor for Macroion Solutions. *Mol. Phys.* **1981**, *42*, 109−118.

(61) Perchiacca, J. M.; Bhattacharya, M.; Tessier, P. M. Mutational Analysis of Domain Antibodies Reveals Aggregation Hotspots within and near the Complementarity Determining Regions. *Proteins* **2011**, *79*, 2637−2647.

(62) Buell, A. K.; Dhulesia, A.; White, D. A.; Knowles, T. P. J.; Dobson, C. M.; Welland, M. E. Detailed Analysis of the Energy Barriers for Amyloid Fibril Growth. *Angew. Chem., Int. Ed.* **2012**, *51*, 5247−5251.

(63) Witten, T. A.; Sander, L. M. Diffusion-Limited Aggregation, a Kinetic Critical Phenomenon. *Phys. Rev. Lett.* **1981**, *47*, 1400−1403.

(64) Weitz, D. A.; Huang, J. S.; Lin, M. Y.; Sung, J. Limits of the Fractal Dimension for Irreversible Kinetic Aggregation of Gold Colloids. *Phys. Rev. Lett.* **1985**, *54*, 1416−1419.

(65) Teixeira, J. Small-Angle Scattering by Fractal Systems. *J. Appl. Crystallogr.* **1988**, *21*, 781−785.

(66) Lattuada, M.; Wu, H.; Morbidelli, M. A Simple Model for the Structure of Fractal Aggregates. *J. Colloid Interface Sci.* **2003**, *268*, 106−120.